




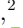

















True mass and atmospheric composition of the non-transiting hot Jupiter HD 143105 b

LUKE FINNERTY ¹ YINZI XIN ² JERRY W. XUAN ² JULIE INGLIS² MICHAEL P. FITZGERALD ¹
SHUBH AGRAWAL ³ ASHLEY BAKER ² RANDALL BARTOS⁴ GEOFFREY A. BLAKE⁵ BENJAMIN CALVIN ^{2,1}
SYLVAIN CETRE⁶ JACQUES-ROBERT DELORME ^{6,2} GREG DOPPMANN⁶ DANIEL ECHEVERRI ² KATELYN HORSTMAN ²
CHIH-CHUN HSU ⁷ NEMANJA JOVANOVIĆ ² JOSHUA LIBERMAN ^{2,8} RONALD A. LÓPEZ ¹ EMILY C. MARTIN ⁹
DIMITRI MAWET^{2,4} EVAN MORRIS⁹ JACKLYN PEZZATO-ROVNER² JEAN-BAPTISTE RUFFIO ¹⁰ BEN SAPPEY ¹⁰
TOBIAS SCHOFIELD² ANDREW SKEMER⁹ TAYLOR VENENCIANO¹¹ J. KENT WALLACE ⁴ NICOLE L. WALLACK ¹²
JASON J. WANG (王劲飞) ⁷ AND JI WANG (王吉) ¹³

¹Department of Physics & Astronomy, 430 Portola Plaza, University of California, Los Angeles, CA 90095, USA

²Department of Astronomy, California Institute of Technology, Pasadena, CA 91125, USA

³Department of Physics and Astronomy, University of Pennsylvania, Philadelphia, PA 19104, USA

⁴Jet Propulsion Laboratory, California Institute of Technology, 4800 Oak Grove Dr., Pasadena, CA 91109, USA

⁵Division of Geological & Planetary Sciences, California Institute of Technology, Pasadena, CA 91125, USA

⁶W. M. Keck Observatory, 65-1120 Mamalahoa Hwy, Kamuela, HI 96743, USA

⁷Center for Interdisciplinary Exploration and Research in Astrophysics (CIERA) and Department of Physics and Astronomy, Northwestern University, Evanston, IL 60208, USA

⁸James C. Wyant College of Optical Sciences, University of Arizona, Meinel Building 1630 E. University Blvd., Tucson, AZ 85721, USA

⁹Department of Astronomy & Astrophysics, University of California, Santa Cruz, CA 95064, USA

¹⁰Center for Astrophysics and Space Sciences, University of California, San Diego, La Jolla, CA 92093

¹¹Physics and Astronomy Department, Pomona College, 333 N. College Way, Claremont, CA 91711, USA

¹²Earth and Planets Laboratory, Carnegie Institution for Science, Washington, DC 20015, USA

¹³Department of Astronomy, The Ohio State University, 100 W 18th Ave, Columbus, OH 43210 USA

(Received December 9, 2024)

ABSTRACT

We present Keck/KPIC phase II K -band observations of the non-transiting hot Jupiter HD 143105 b. Using a cross-correlation approach, we make the first detection of the planetary atmosphere at $K_p = 185_{-13}^{+11}$ km s⁻¹ and an inferior conjunction time 2.5 hours before the previously-published ephemeris. The retrieved K_p value, in combination with orbital period, mass of the host star, and lack of transit detection, gives an orbital inclination of 78_{-12}^{+2} and a true planet mass of 1.23 ± 0.10 M_J. While the equilibrium temperature of HD 143105 b is in the transition regime between non-inverted and inverted atmospheres, our analysis strongly prefers a non-inverted atmosphere. Retrieval analysis indicates the atmosphere of HD 143105 b is cloud-free to approximately 1 bar and dominated by H₂O absorption ($\log \text{H}_2\text{O}_{\text{MMR}} = -3.9_{-0.5}^{+0.8}$), placing only an upper limit on the CO abundance ($\log \text{CO}_{\text{MMR}} < -3.7$ at 95% confidence). We place no constraints on the abundances of Fe, Mg, or ¹³CO. From these abundances, we place an upper limit on the carbon-to-oxygen ratio for HD 143105 b, C/O < 0.2 at 95% confidence, and find the atmospheric metallicity is approximately $0.1 \times$ solar. The low metallicity may be responsible for the lack of a thermal inversion, which at the temperature of HD 143105 b would likely require significant opacity from TiO and/or VO. With these results, HD 143105 b joins the small number of non-transiting hot Jupiters with detected atmospheres.

Corresponding author: Luke Finnerty

lfinnerty@astro.ucla.edu

Keywords: Exoplanet atmospheres (487) — Exoplanet atmospheric composition (2021) — Hot Jupiters (753) — High resolution spectroscopy (2096)

1. INTRODUCTION

Transmission and secondary eclipse spectroscopy are powerful tools for characterizing exoplanet atmospheres, but are fundamentally limited to the small fraction of planets which transit their host stars. By directly detecting planetary dayside emission, high-resolution cross-correlation spectroscopy (HRCCS) techniques can be used to characterize the atmospheres of non-transiting exoplanets (e.g. Brogi et al. 2012; Rodler et al. 2012; Brogi et al. 2014; Birkby et al. 2017; Guilluy et al. 2019; Webb et al. 2020; Buzard et al. 2020; Pelletier et al. 2021). These observations break the mass-inclination degeneracy from the radial velocity technique and enable constraints on the true mass of non-transiting planets. The significant inclinations of some of these systems may also enable novel characterization of the polar regions of hot Jupiters (Malsky et al. 2021).

High-resolution spectroscopy of non-transiting planets must contend with additional uncertainties compared with observations of transiting targets, increasing the risks associated with these observations. For planets with nearly face-on orbits, the projected line-of-sight velocity shift may be too small compared to the instrument resolution to make a detection, even if the planet would be detectable if the orbit were edge on. The observed velocity shift decreases with $\sin i$, so this effect is prohibitive for a relatively small fraction of non-transiting planets, but necessitates additional care when scheduling observations so that a sufficient velocity shift will be obtained even if the system is low inclination.

Additionally, non-transiting planets have ephemerides based on radial velocity observations alone. While transiting planets detected with TESS often have periods and transit times determined to a precision of seconds, such precise ephemerides are difficult to achieve for non-transiting planets. Furthermore, maintaining current ephemerides via radial velocity monitoring requires significant investments of telescope time, and as a result many non-transiting systems do not have recently updated ephemerides. This can lead to significant uncertainty in the orbital phase for followup HRCCS observations.

These challenges have limited the number of non-transiting planets detected via HRCCS. τ Boo b was the first non-transiting planet detected with HRCCS by Brogi et al. (2012), followed by HD 179949 b (Brogi et al. 2014). Brogi et al. (2013) reported a tentative detection of 51 Peg b which was confirmed by Birkby et al.

(2017), and HD 102195 b was first reported in Guilluy et al. (2019). HD 187123 b was detected via a similar technique by Buzard et al. (2020). This is only a small fraction of the number of transiting systems characterized with HRCCS techniques.

HD 143105 b is a non-transiting hot Jupiter first detected in 2016 using radial velocity observations from the SOPHIE spectrograph (Hébrard et al. 2016). Properties of the system are summarized in Table 1. While the short orbital period and bright host star make HD 143105 b a good candidate for atmospheric characterization, the far-northern declination of the system has made it inaccessible to most ground-based high-resolution spectrographs, and *JWST* has so far only characterized hot Jupiters using transmission and eclipse methods, leaving HD 143105 b unstudied. HD 143105 b is a particularly interesting target for atmospheric characterization, as its 1940 K equilibrium temperature is close to the expected transition between atmospheres with and without a thermal inversion predicted by both 1D (Baxter et al. 2020) and 3D modeling (Roth et al. 2024). In this paper, we use Keck/KPIC HRCCS observations to make the first atmospheric detection of HD 143105 b which enables us to refine the planetary ephemeris and constrain the atmospheric composition and pressure-temperature ($P - T$) profile.

We discuss the Keck/KPIC observations of HD 143105 b and our atmospheric retrieval framework in Section 2. Results from the cross-correlation and retrieval analyses are presented in Section 3, and discussed in Section 4. Section 5 concludes.

2. OBSERVATIONS AND DATA REDUCTION

2.1. Observations

The HD 143105 system was observed using Keck II/KPIC phase II (McLean et al. 1998; Martin et al. 2018; López et al. 2020; Delorme et al. 2021; Echeverri et al. 2022) for the first half of the night on UT 24 May 2024, from 6:24 to 10:19. The observations were scheduled around a predicted superior conjunction based on the Hébrard et al. (2016) ephemeris in order to maximize dayside visibility and velocity shift of the planet over the observation. The maximum velocity shift was estimated to be 80 km s^{-1} for a 90 degree inclination, sufficient to allow detection of the planet even if a significant orbital inclination resulted in a much smaller change in the projected velocity over the course of the

Property	Value	Ref.
HD 143105		
RA	15:53:36.57	Gaia Collaboration (2020)
Dec	+68:43:11.92	Gaia Collaboration (2020)
Sp. Type	F5	Hébrard et al. (2016)
K_{mag}	5.52 ± 0.02	Cutri et al. (2003)
Mass	$1.51 \pm 0.11 M_{\odot}$	Hébrard et al. (2016)
Radius	$1.61^{+0.08}_{-0.05} R_{\odot}$	ExoFOP (2019)
T_{eff}	6380 ± 60 K	Hébrard et al. (2016)
$\log g$	4.37 ± 0.04	Hébrard et al. (2016)
$v \sin i$	9.1 ± 1 km s ⁻¹	Hébrard et al. (2016)
v_{rad}	15.942 ± 0.003 km s ⁻¹	Hébrard et al. (2016)
[Fe/H]	0.05 ± 0.04	Hinkel et al. (2014)
[C/H]	0.03 ± 0.34	Hinkel et al. (2014)
[O/H]	0.02 ± 0.04	Hinkel et al. (2014)
HD 143105 b		
Period	2.1974 ± 0.0003 days	Hébrard et al. (2016)
T_{conj}	JD 2456531.344 \pm 0.007	Hébrard et al. (2016)
T_{conj}	JD 2456531.237 ^{+0.012} _{-0.017}	This work
a	0.0379 ± 0.0009 AU	Hébrard et al. (2016)
e	< 0.07	Hébrard et al. (2016)
i	78^{+2}_{-12}	This work
K_{p}	185^{+11}_{-13} km s ⁻¹	This work
$M \sin i$	$1.21 \pm 0.06 M_{\text{J}}$	Hébrard et al. (2016)
Mass	$1.23 \pm 0.10 M_{\text{J}}$	This work
Radius	$1.20 \pm 0.05 R_{\text{J}}$	Assumed
T_{eq}	1940 K	Calculated
C/O	< 0.4	This work
[C/H]	< -1.1	This work
[O/H]	$-1.3^{+0.9}_{-0.5}$	This work
$v \sin i$	$7.4^{+3.1}_{-3.5}$ km s ⁻¹	This work

Table 1. Stellar and planetary properties for the HD 143105 system. Upper limits from this work are given at 95% confidence, omitting the secondary mode for the C/O ratio.

observation. Exposures were taken staring on KPIC science fiber 2 with a 90 second integration time in order to avoid saturation on the NIRSPEC detector.

Weather conditions were sub-optimal throughout the observation. Telescope opening was delayed by approximately 40 minutes at the start of the night due to high humidity, which persisted throughout the night. Cloud cover was variable throughout the observations, which resulted in brief periods of extinction up to two magnitudes. The observation sequence began as HD 143105 was rising, at an airmass of 1.93, and continued un-

til the target was just past transit, at an airmass of 1.51. Despite the high airmass, the top-of-atmosphere throughput to KPIC was consistently $\sim 2.5\%$ during clear periods, consistent with the median KPIC phase II performance (Echeverri et al. 2022, Jovanovic et al. in prep.). This is a significant improvement in instrument performance over previous high-airmass observations taken under better atmospheric conditions. This improvement is likely as a result of recent upgrades to the real-time controller for the Keck AO system providing better AO and differential refraction corrections at high airmass.

2.2. Data Reduction

Similar to previous KPIC observations (e.g. Finnerty et al. 2023, 2024), we observed a late-type star to provide additional stellar lines for wavelength calibration, in this case HIP 62944. The 1D spectrum was extracted and used to fit a wavelength solution following the standard KPIC Data Reduction Pipeline (DRP)¹.

For the observations of HD 143105, we used the LSF fitting procedure described in Finnerty et al. (subm.), which handles the non-Gaussian wings and wavelength-dependence of the KPIC trace using a Gaussian-Hermite model to produce weights for optimal extraction. For the LSF, we scale the overall width of the resulting spatial profile by a factor of 1.14, as was previously done in Finnerty et al. (subm.), based on the spatial/spectral width asymmetry reported in Finnerty et al. (2022). This LSF kernel is then convolved with the forward model of the planetary spectrum after the rotational broadening kernel is applied and prior to the calculation of the log likelihood. In theory, this technique should enable constraints on $v \sin i$ better than the 9 km s⁻¹ resolution of the Keck/NIRSPEC spectrograph, although in practice systematic uncertainties in the LSF make physical interpretation of such small rotational velocities suspect.

Following extraction, we coadded each consecutive pair of science frames in order to boost signal-to-noise and reduce the data volume for retrieval. The final extracted SNR per wavelength channel was approximately 265 in the bluest order included in analysis and 166 in the reddest order. The decreased SNR at longer wavelengths is due to a combination of atmospheric dispersion and increased thermal background at the red end of the K -band.

Consistent with previous KPIC observations, orders 37–39, covering 1.94–2.09 μm , are heavily contaminated

¹ https://github.com/kpicteam/kpic_pipeline/

by telluric features and omitted from subsequent analysis. Initial cross-correlation analysis found that orders 35 and 36 do not meaningfully contribute to the planet detection due to the absence of strong spectral features. We therefore restrict our analysis to orders 31–34, spanning 2.22–2.49 μm , in order to speed up retrievals.

2.3. Cross-correlation

Propagating the reported period uncertainty from Hébrard et al. (2016) to the observation epoch results in an uncertainty of approximately 12 hours in the conjunction time. We therefore began with a cross-correlation analysis in order to isolate the planet signal for subsequent retrieval. Rather than varying the planet RV semi-amplitude K_p and the systemic velocity v_{sys} , we instead vary K_p and the conjunction time, ΔT_{conj} . This better reflects existing knowledge of a system where the inclination is unknown and the orbital phase has significant uncertainties, but the systemic velocity is well-constrained by previous radial velocity observations. In particular, the short orbital period of HD 143105 b creates a scenario where a change in orbital phase corresponding to just a few hours can dramatically change the velocity track of the planet, from nearly linear in the case of observations near conjunction to clearly sinusoidal for phases close to quadrature.

To create the $K_p - \Delta T_{conj}$ plots, we projected out 6 principal components during detrending, and computed the cross-correlation rather than the log-likelihood. The Brogi & Line (2019) log-likelihood function shows strong systematic effects in the $K_p - \Delta T_{conj}$ space due to its explicit dependence on the model variance. As a result of the time series detrending and its replication in the forward modeling, the model variance is itself strongly dependent on the velocity shift of the planet, which changes with both K_p and ΔT_{conj} . The cross-correlation coefficient is much less dependent on the variance of the planet models, making it a more appropriate choice for detection in this case. See Finnerty et al. (2024) for a more extended discussion of these systematics in the $K_p - v_{sys}$ case.

2.4. Atmospheric Retrieval

We continue to use the retrieval framework described in Finnerty et al. (2023, 2024, Finnerty et al., submitted), with some minor updates which we summarize below. Our retrievals now use `petitRADTRANS` version 3 (Mollière et al. 2019, 2020; Nasedkin et al. 2024), which significantly improves the efficiency of the radiative transfer calculation. We also add a grey cloud opacity, following the `petitRADTRANS` documentation:

$$\kappa_{\text{cld}} = \kappa_{0,\text{cld}} (P/P_0)^{f_{\text{SED}}} \quad (1)$$

which is applied for $P > P_0$. We treat P_0 , $\kappa_{0,\text{cld}}$, and f_{SED} as free parameters in the retrieval.

Additionally, we have changed the PCA to be performed on the temporal axis of the data arrays, rather than the spectral axis. This provides a minor performance improvement, and does not change the resulting log-likelihood for small numbers of omitted components. The resulting principal component vectors are also somewhat easier to interpret, representing the way the observed spectrum evolves in time, rather than expressing the time series as a sum of component spectra with time-varying weights.

Based on the ephemeris uncertainty discussed previously, we opt to update the nominal T_{conj} for the retrieval analysis to JD 2456531.2225 based on the mean offset in from the four models shown in Figure 1. We then fit for a small offset in the conjunction time in the retrieval, rather than v_{sys} . This offset corresponds to a ± 1.2 hour shift in the conjunction time, which was chosen based on the range of offsets from Figure 1.

Finally, we have changed the nested sampling implementation from `dynesty` (Speagle 2020) to `MultiNest` (Feroz & Hobson 2008; Feroz et al. 2009; Buchner et al. 2014; Feroz et al. 2019). Both packages produce similar final posteriors, but `MultiNest` is approximately 10 \times faster, enabling retrievals in 12 hours of wall time with 8 CPU cores. We use 500 live points and a $\Delta \log z < 0.1$ convergence criteria. The final posteriors are consistent with runs using a larger number of live points and/or a stricter convergence criteria (e.g. 1000 or 1200 live points, $\Delta \log z < 0.01$), but the smaller number of live points and looser $\Delta \log z$ criteria significantly reduce the total run time.

The equilibrium temperature of HD 143105 b estimated with the system properties listed in Table 1 is ~ 1940 K. This is close to the transition temperature where models predict dayside thermal inversions (e.g. Baxter et al. 2020; Roth et al. 2024). We therefore choose a wide prior on the γ parameter of the of the Guillot (2010) Pressure-Temperature ($P - T$) profile to permit either inverted or non-inverted atmospheres. While the internal temperature parameter T_{int} has not been well-constrained in previous retrievals of hot Jupiter atmospheres with KPIC data, we include it as a free parameter for completeness, and similarly include the planetary surface gravity $\log g$ as a free parameter. Tests using the `easyCHEM` (Mollière et al. 2017; Lei & Mollière 2024) equilibrium chemistry calculator indicate the dominant metal species at the expected temperatures in the atmosphere of HD 143105 b are CO, H₂O, Fe, and Mg, and that the vertical mixing profiles for these species are nearly constant with altitude for the

non-inverted $P - T$ profiles favored in the initial cross-correlation analysis. We therefore treat all abundances as constant with altitude.

For the molecular species, we use the opacity tables previously described in Finnerty et al. (2023). For H_2O , these tables used the (Polyansky et al. 2018) partition function and HITEMP 2010 linelist (Rothman et al. 2010). For both CO isotopologues we used the HITEMP 2019 lists (Gordon et al. 2022) and the Li et al. (2015) partition function. For Fe and Mg we use the `petitRADTRANS` provided tables based on the Kurucz atomic line lists.

We ran retrievals omitting 4, 6, and 8 principal components during the data detrending process. We report the values from the 6 component retrieval in Section 3. The marginalized medians and confidence intervals are consistent between all three retrievals, indicating the values we report are not strongly dependent on the number of PCA components.

3. RESULTS

3.1. Cross-correlation Analysis

For the initial cross-correlation analysis, we generated models based on the equilibrium temperature of HD 143105 b and varying assumed compositions under chemical equilibrium. For the $P - T$ profile, we assumed $\log \kappa = -1$, $\log \gamma = -1$ for the non-inverted case and $\log \gamma = 1$ for the inverted case, $\log g = 3.3$, $T_{\text{int}} = 100$ K, and $T_{\text{eq}} = 1940$ K. The assumed cloud parameters were $f_{\text{SED}} = 4$, $\log \kappa_{0,\text{cld}} = 1$, $\log P_{\text{cloud}} = 0$. We assumed planetary $v \sin i = 3 \text{ km s}^{-1}$, corresponding to tidally-locked rotation for a planetary radius of $1.2R_{\text{J}}$, consistent with a moderately inflated hot Jupiter. For the molecular abundances, we used `easychem` (Mollière et al. 2017; Lei & Mollière 2024) to compute equilibrium abundance profiles for H_2O , CO, Fe, and Mg assuming different atmospheric C/O ratios (0.3 or 0.8), metallicities (-0.3 or +0.3 dex relative to solar), and whether or not a thermal inversion is present, for a total of eight planet models. For the inverted models, we did not account for vertical variations in species abundances, although `easychem` predicts H_2O dissociates above the inversion and Fe and Mg are not present in significant quantities below the inversion. We instead took the respective lower/upper atmosphere abundances as constant. While this would create model mismatches in a retrieval analysis, it should not preclude simple detection.

3.1.1. Ephemeris and velocities

Figure 1 shows the computed $K_p - \Delta T_{\text{conj}}$ plots for the four non-inverted planet models, while Figure 2

shows the four inverted models. Figure 3 shows the $K_p - v_{\text{sys}}$ diagram for a non-inverted model with both the Hébrard et al. (2016) and our revised ephemerides for comparison. All four non-inverted models show a $\text{SNR} \sim 4$ feature at approximately $\Delta T_{\text{conj}} = -180$ minutes, $K_p = 167 \text{ km s}^{-1}$. None of the inverted models produce features of comparable strength, and all of the inverted models are consistent with a non-detection, indicating that the observed planet flux is primarily arising from regions without a thermal inversion. Based on the reported semi-major axis and orbital period from Hébrard et al. (2016), the maximum value for K_p , corresponding to a 90 degree inclination, is $188 \pm 4 \text{ km s}^{-1}$, so the $K_p = 167 \text{ km s}^{-1}$ value from the non-inverted models is consistent with a detection of the non-transiting HD 143105 b. The ΔT_{conj} offset is consistent with the expected uncertainty from propagating the Hébrard et al. (2016) uncertainty in the orbital period to the observation epoch. While there are slight shifts in the location of the cross-correlation peak for different non-inverted models, these shifts are relatively small and consistent with the strong degeneracy between K_p and ΔT_{conj} .

We use the scale of the K_p and ΔT_{conj} offsets to inform the priors used for atmospheric retrieval. We update the nominal conjunction time to $T_{\text{conj}} = \text{JD } 2456531.2225$ and the nominal K_p to 167 km s^{-1} . We use these values for the remaining analysis.

3.1.2. Molecular detections

Plots of $K_p - \Delta T_{\text{conj}}$ for the the $[\text{M}/\text{H}] = 0.3$, $\text{C}/\text{O} = 0.8$ model, and individually for CO, H_2O , and Mg+Fe, are shown in Figure 4. We use the same $P - T$ parameters throughout, and base abundances on the $[\text{M}/\text{H}] = 0.3$, $\text{C}/\text{O} = 0.8$ model, which produced the strongest detection in Figure 1.

Only H_2O produces a significant detection in isolation. The CO model shows a weak peak consistent with the planet velocity from the H_2O model, but other features dominate the cross-correlation space. The refractory species do not produce any discernible peak near the expected planet velocity, and the cross-correlation space for these species is dominated by a feature in the stellar rest frame as a result of Fe and Mg lines in the stellar atmosphere. However, the all-molecule case is better detected than any individual molecules. This suggests that CO and the refractory species may be contributing some improvement to the overall detection, even if they are not independently detected in the absence of H_2O .

The absence of a significant CO detection appears to be at odds with the slight preference for high C/O from the initial cross-correlation analysis, shown in Figure 1.

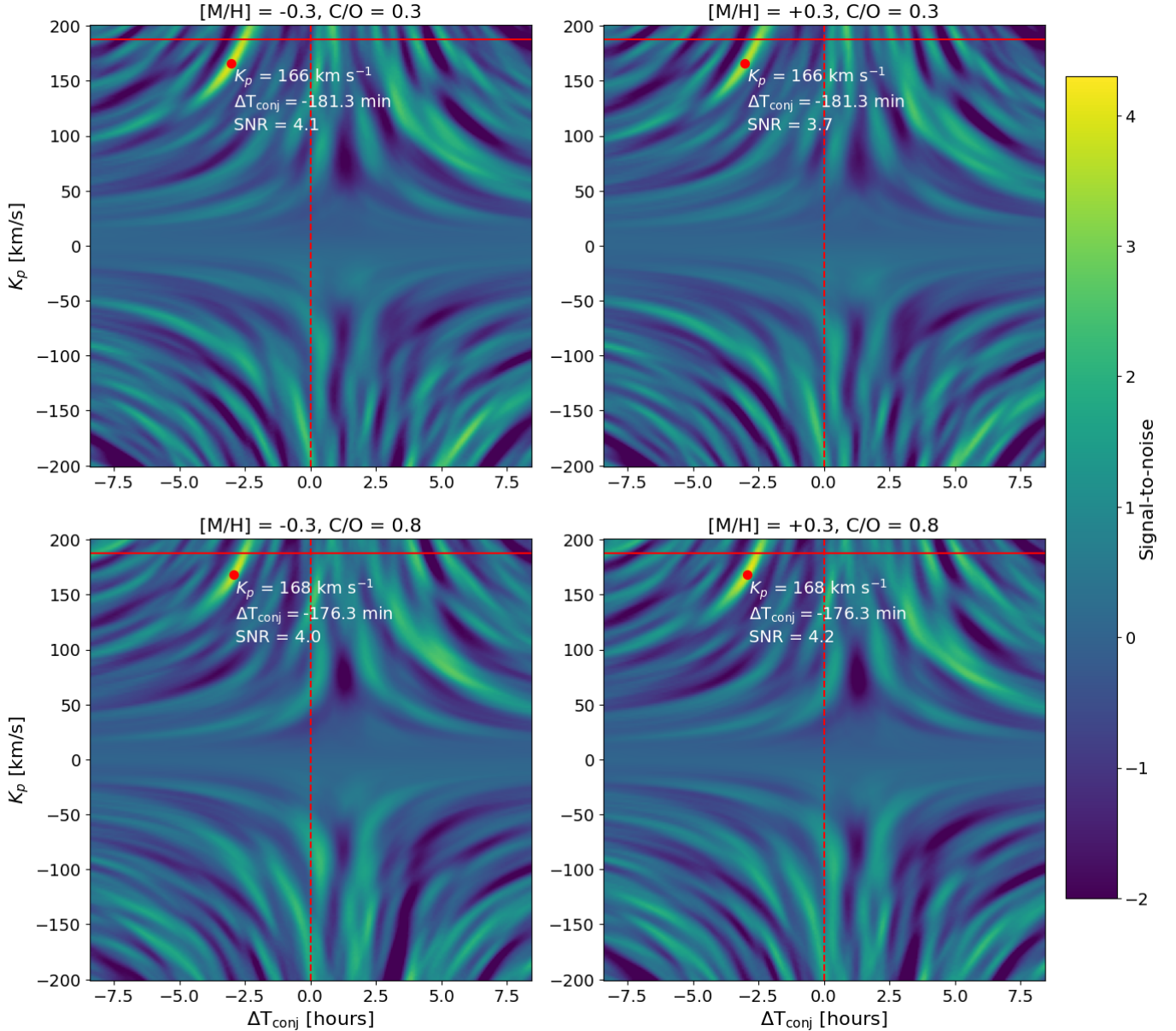


Figure 1. K_p vs conjunction time offset the four non-inverted planet models with varying metallicity and C/O ratio. All four models show a strong feature consistent with a planet detection at similar K_p and ΔT_{conj} . The peak values correspond to a conjunction time approximately 3 hours before the expectation from Hébrard et al. (2016), well within the propagated uncertainty in the conjunction time arising from uncertainty in the orbital period. The peak planet RV semi-amplitude is $\sim 167 \text{ km s}^{-1}$ for all models, corresponding to an inclination of 64 degrees. The signal-to-noise was calculated by dividing the map by the standard deviation of the $K_p < -60$ region. All models are detected at similar strength.

However, we note that the increase in detection strength over the low C/O models in Figure 1 is marginal, and estimating the noise level for the $K_p - \Delta T_{\text{conj}}$ diagram signal-to-noise by taking the off-peak cross-correlation variance has some associated uncertainty. Furthermore, the large number of H_2O lines in the K -band leads to a pseudocontinuum in the planet model which differs significantly from a blackbody, which may lead to worse detections when using single-molecule templates omit-

ting H_2O (Finnerty et al. 2024). As a result, we rely on the Bayesian retrieval analysis to constrain the chemical composition, rather than the cross-correlation.

3.2. Retrieval Analysis

Priors, maximum-likelihood parameters, and retrieved medians with $\pm 34\%$ confidence intervals are presented in Table 2. Our free-chemistry approach does not directly fit for $[C/H]$, $[O/H]$, or C/O, but we use the retrieved

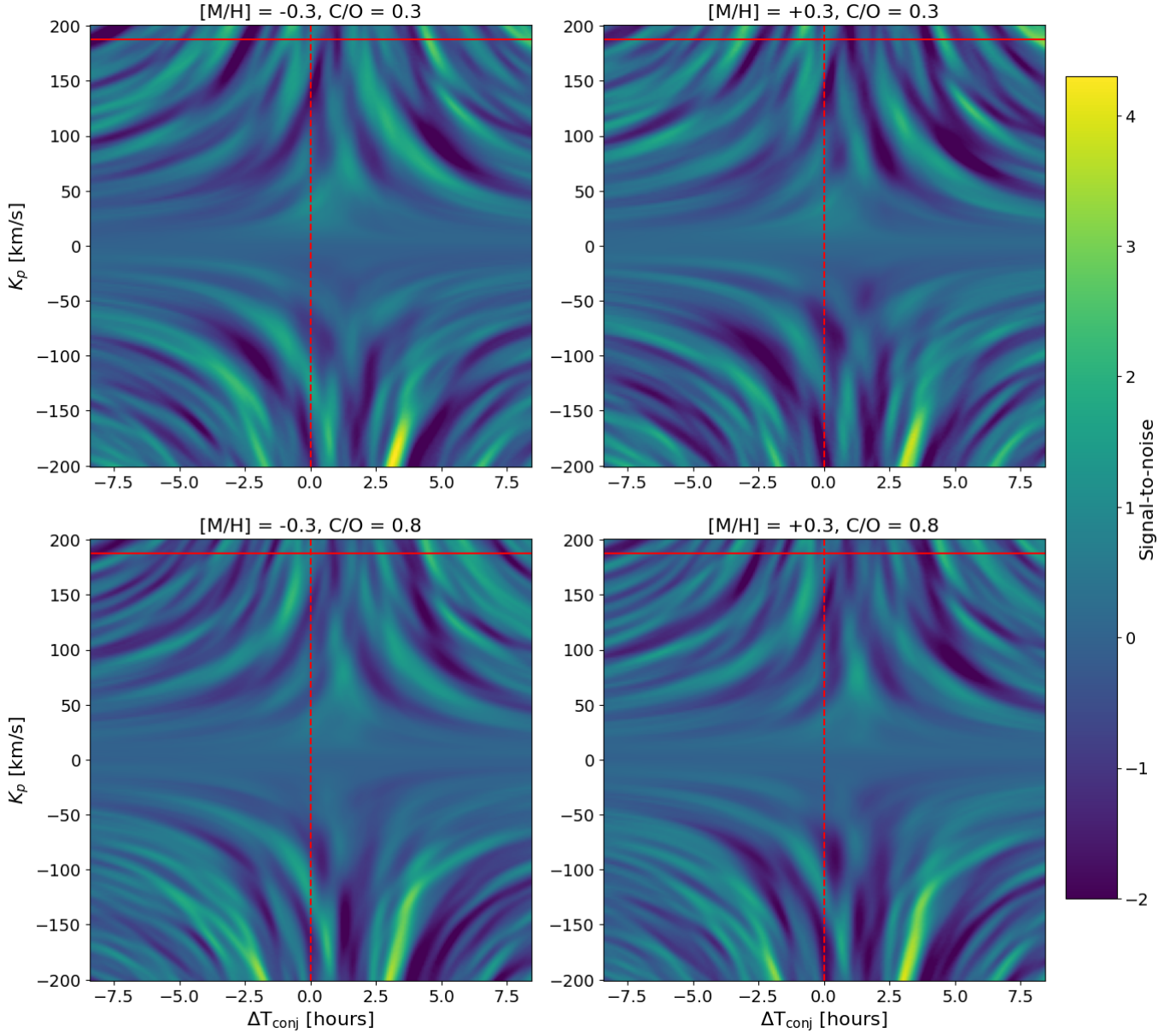


Figure 2. K_p vs conjunction time offset for the four inverted planet models with varying metallicity and C/O ratio. None of these models give a potential planet detection in the region permitted by the prior ephemeris, indicating the detected planet flux is primarily arising from regions of the planetary atmosphere without a thermal inversion. The peak at $T_{\text{conj}} = +2.5$ hours, $K_p = -175 \text{ km s}^{-1}$ corresponds to a velocity track near transit/inferior conjunction, when the observed disk is dominated by the nightside of the planet. As this is incompatible with the previous ephemeris constraints, and we expect the nightside atmosphere to be non-inverted, we believe this feature arises from cross-talk with stellar residuals and is not related to the planetary atmosphere.

posteriors to construct posteriors for these parameters, and report the corresponding values in Table 2 as derived parameters. We present the results of the retrieval omitting 6 principal components. The medians and confidence intervals for the 4 and 8 component cases did not significantly differ from the values reported in Table 2.

3.2.1. Kinematics

The retrieved K_p and ΔT_{conj} are slightly offset compared with the values from the cross-correlation analysis shown in Figure 1 and 4, but are consistent with the degeneracy between these parameters. The prior on ΔT_{conj} corresponds to a ± 1.2 hour change in the conjunction time, based on the apparent extent of the planet

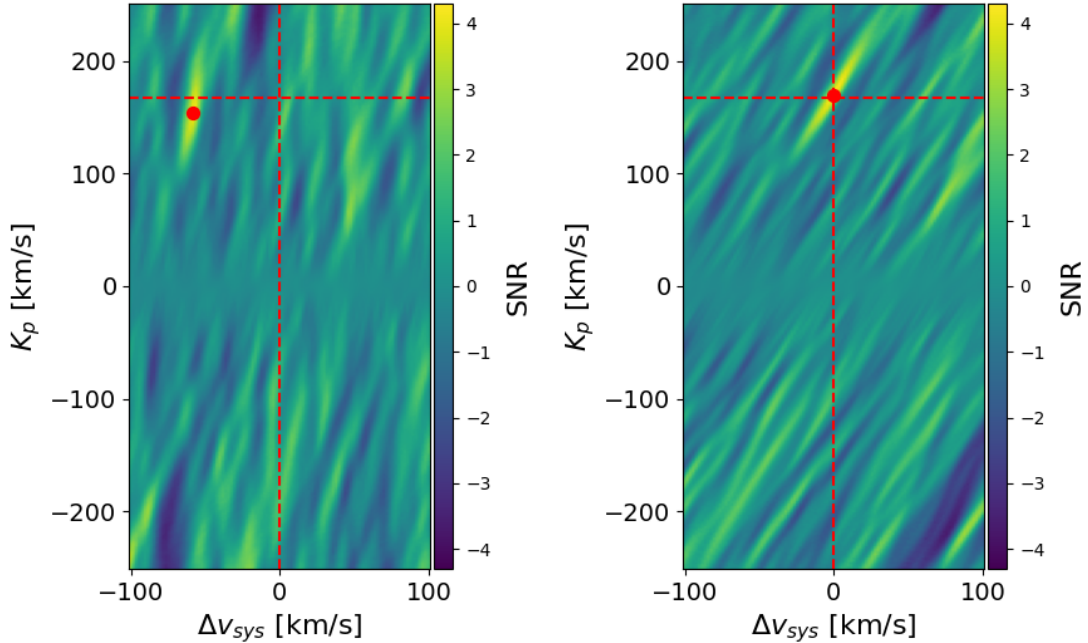


Figure 3. $K_p - v_{sys}$ diagrams for the Hébrard et al. (2016) ephemeris (left) and the revised ephemeris based on Figure 1 (right). The $Z = 0.3$, $C/O = 0.8$, non-inverted model was used in both cases. The Hébrard et al. (2016) ephemeris produces a detection of comparable strength, but with $\Delta v_{sys} = -60 \text{ km s}^{-1}$, well outside the expected range of offsets for a planet with a well-constrained ephemeris.

peak in 1, and ΔT_{conj} is well-constrained to within ~ 25 minutes.

The retrieval provides a weak constraint on the planetary rotational velocity, $v \sin i = 7.4^{+3.1}_{-3.5} \text{ km s}^{-1}$. This is comparable to the spectrograph resolution, corresponding to a $\sim 30\%$ broadening of the planet lines compared with the instrumental profile alone. The expected $v \sin i$ for tidally-locked rotation is $\sim 3 \text{ km s}^{-1}$, leaving $\sim 5 \text{ km s}^{-1}$ of unexplained broadening. This could be consistent with apparent broadening from a broadly-distributed westward-flowing wind pattern, similar to that reported for other hot and ultra-hot Jupiters (e.g. Pai Asnodkar et al. 2022; Gandhi et al. 2023). However, the poor quality of the $v \sin i$ constraint and uncertainties in the true LSF preclude a definitive physical interpretation of this value.

We used the same line-spread treatment as that developed in Finnerty et al. (subm.), and have the same systematic uncertainty in the overall LSF width at the $\sim 10\%$ level. While the retrieved broadening is somewhat larger than we believe could be explained solely by a systematic error in the LSF, we are cautious about making specific quantitative or physical interpretations of the retrieved broadening, particularly given the broad marginalized posterior for $v \sin i$. Higher-resolution observations, particularly from instruments with robust LSF calibration (as is planned for Keck/HISPEC, Mawet et al. (2019)), are necessary to quantitatively in-

terpret line broadening in planetary atmospheres. A $v \sin i$ of 7 km s^{-1} would be $> 2\times$ the spectral resolution of Keck/HISPEC, and should be easily distinguishable.

3.2.2. Pressure-temperature profile and clouds

The retrieved $P - T$ profile and emission contribution function are shown in Figure 5. The retrieved $P - T$ profile is non-inverted and somewhat colder than expected based on the equilibrium temperature of 1940 K. This is consistent with previous KPIC retrievals (Finnerty et al. 2023, 2024, Finnerty et al., submitted). As with these previous results, the overall scaling factor applied to the planet model is > 1 , compensating for the lower temperature. Broader wavelength coverage that covers a significant change in the planet continuum flux (such as the region surrounding the blackbody peak) would break this degeneracy.

Of the cloud parameters, only the pressure is constrained. The retrieved pressure is quite deep, with the posterior peaking around 2.5 bar, well below the bottom of the emission contribution function shown in Figure 5. At these pressures, the final impact on the outgoing planet flux is negligible, so f_{SED} and $\kappa_{0, \text{cl}}$ are unconstrained, and the atmosphere over the pressure range probed by the K -band observations is effectively clear.

3.2.3. Chemical composition

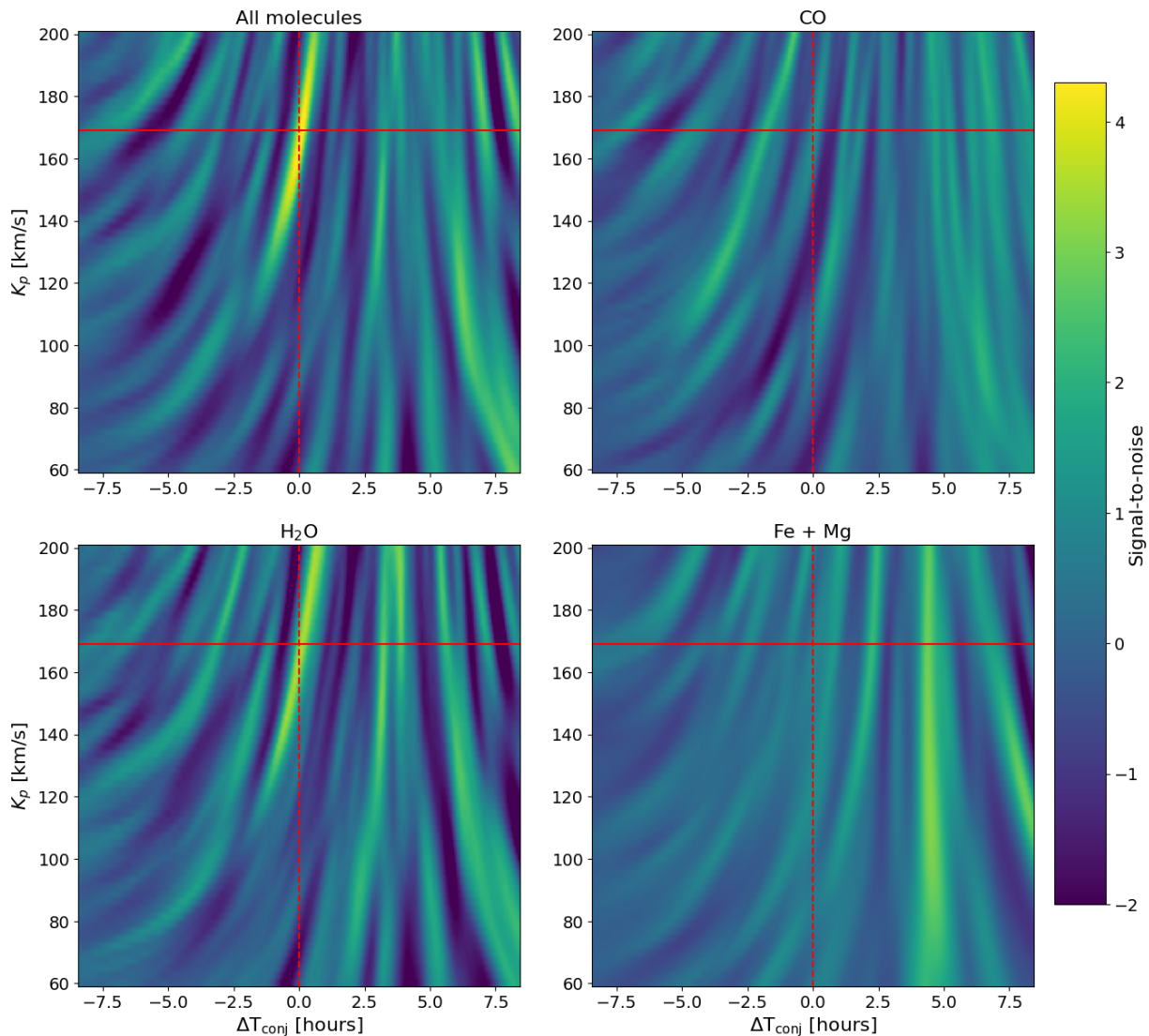


Figure 4. K_p vs conjunction time offset for models of all species, CO, H₂O, and Fe+Mg, with abundances based on the non-inverted $[M/H] = 0.3$, $C/O = 0.8$ model which produced the strongest detection in Figure 1. The conjunction time has been updated based on the measured offsets from Figure 1, so planetary features should appear at approximately $K_p = 167$ km s⁻¹, $\Delta T_{\text{conj}} = 0$ hours. Only H₂O is confidently detected. A weak feature is present at the same location with the CO model, but does not dominate the $K_p - \Delta T_{\text{conj}}$ space and does not constitute an independent detection. The refractory species are not detected.

Consistent with the cross-correlation analysis, the retrieval provides a bounded constraint only for the H₂O abundance, $\log H_2O = -3.9^{+0.8}_{-0.5}$. While the maximum likelihood value for the CO mass fraction is $\log CO = -4.7$, the retrieval does not provide a lower bound on the CO abundance. High CO abundances are strongly excluded ($\log CO_{MMR} < -3.7$ at 95% confidence). As a result, while the maximum-likelihood C/O ratio is 0.1, the median value from the retrieval is consistent with 0. This outcome could be explained by a CO abundance at or just below the detection limit of our observations. The CO isotopologue ratio is entirely unconstrained,

consistent with the non-detection of the primary isotopologue.

The refractory species abundances are entirely unconstrained. While other K -band observations (e.g. Ramkumar et al. 2023) have been able to constrain Fe abundances in hot Jupiter atmospheres, we suspect that the lower spectral resolution of NIRSPEC is insufficient to make a detection based on the small number of accessible Fe and Mg lines (see Figure 5, bottom panel).

4. DISCUSSION

4.1. Ephemeris revision and true mass

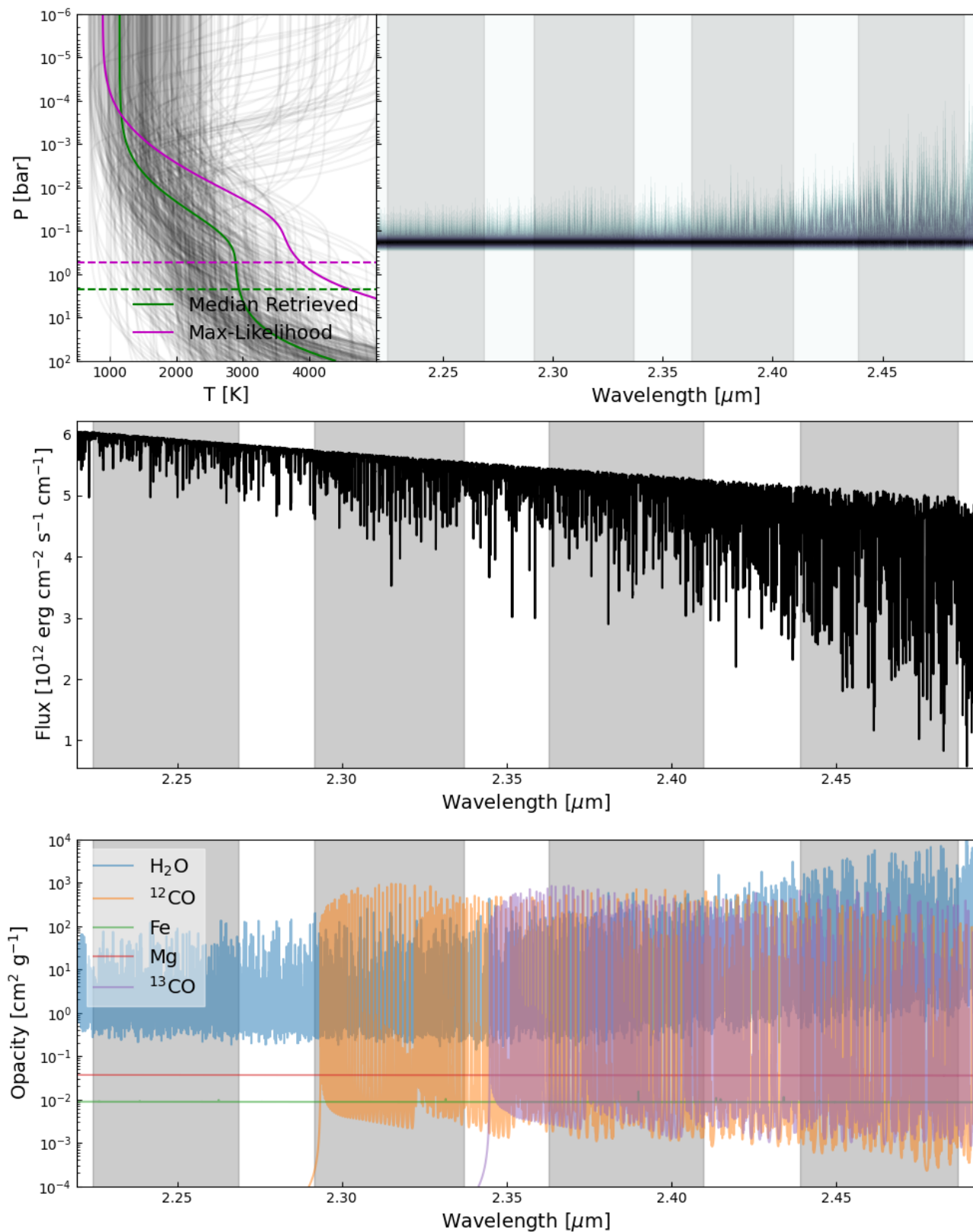


Figure 5. Retrieved $P - T$ profile (top left), maximum-likelihood emission contribution function (top right), maximum-likelihood spectrum (middle), and species opacities (bottom). In the $P - T$ plot, the median retrieved profile is shown in green, and the maximum likelihood profile in purple. The cloud pressures are indicated by horizontal dashed lines. The black lines are the $P - T$ profiles from 500 draws from the retrieved posteriors. In the emission contribution function, spectrum, and opacity panels, the observed orders are shaded in grey. Most of the emission arises between 1 bar and 30 mbar, where the $P - T$ profile begins to cool, and is significantly above the cloud pressure, indicating the atmosphere is clear at the pressures probed by these K -band observations. The maximum-likelihood spectrum shows weak CO features in addition to H_2O , and the non-detection of refractory species is consistent with the extremely low opacity of these species in comparison to CO and H_2O .

Name	Symbol	Prior	Retrieved Max-L	Retrieved Median
log infrared opacity [cm^2g^{-1}]	$\log \kappa$	Uniform(-3, 3)	-1.9	$-1.2^{+1.0}_{-0.9}$
log infrared/optical opacity	$\log \gamma$	Uniform(-3, 3)	-2.5	$-1.7^{+0.7}_{-0.7}$
Intrinsic temperature [K]	T_{int}	Uniform(50, 1000)	410	< 800
Equilibrium temperature [K]	T_{equ}	Uniform(800, 3000)	1100	1400^{+400}_{-300}
log surface gravity [cgs]	$\log g$	Uniform(2,4)	2.2	$3.0^{+0.6}_{-0.6}$ *
Cloud opacity index	f_{SED}	Uniform(0,8)	7.9	$4.8^{+2.0}_{-2.1}$ *
Cloud base opacity	$\log \kappa_0$	Uniform(0,3)	1.5	$1.5^{+1.0}_{-0.9}$ *
Cloud base pressure	$\log P_{\text{cloud}}$	Uniform(-4,2)	-0.3	> -1.7
K_p offset [km s^{-1}]	ΔK_p	Uniform(-40, 40)	12.8	$17.9^{+10.6}_{-13.2}$
Conjunction time offset [hours]	ΔT_{conj}	Uniform(-1.2, 1.2)	0.27	$0.47^{+0.24}_{-0.28}$
Rotational velocity [km s^{-1}]	v_{rot}	Uniform(0, 15)	5.8	$7.4^{+3.1}_{-3.5}$ *
log H ₂ O mass-mixing ratio	$\log \text{H}_2\text{O}$	Uniform(-12, -0.5)	-3.9	$-3.9^{+0.8}_{-0.5}$
log CO mass-mixing ratio	$\log \text{CO}$	Uniform(-12, -0.5)	-4.7	< -3.7
log Fe mass-mixing ratio	$\log \text{Fe}$	Uniform(-12,-1)	-4.1	$-6.5^{+3.3}_{-3.4}$ *
log Mg mass-mixing ratio	$\log \text{Mg}$	Uniform(-12,-1)	-1.6	$-6.6^{+3.4}_{-3.2}$ *
log ¹³ CO/ ¹² CO	$\log^{13}\text{CO}_{\text{rat}}$	Uniform(-8, -0.5)	-5.1	$-4.2^{+2.3}_{-2.2}$ *
log H mass-mixing ratio	$\log \text{allH}$	Uniform(-0.4, -0.05)	-0.2	$-0.2^{+0.1}_{-0.1}$ *
Scale factor	scale	LogNormal(0, 0.2)	0.4	$0.2^{+0.2}_{-0.2}$
Derived Parameters				
Carbon/oxygen ratio	C/O	-	0.1	< 0.2
Carbon abundance	[C/H]	-	-2.1	< -1.1
Oxygen abundance	[O/H]	-	-1.3	$-1.3^{+0.9}_{-0.5}$
Volatile abundance	[(C+O)/H]	-	-1.5	$-1.5^{+0.9}_{-0.5}$

Table 2. List of parameters, priors, and results for atmospheric retrievals. The error bars on the retrieved medians correspond to the 68%/1 σ confidence interval. Limits are given at 95% confidence, omitting the secondary mode for the C/O ratio

. A * indicates the marginalized posterior for a parameter is unconstrained (i.e. the marginalized posterior spans the full range of the prior). In addition to these priors, we required that the atmospheric temperature stay below 6000 K at all pressure levels. The full corner plot is included in Appendix A.

Our analysis indicates the inferior conjunction of HD 143105 b prior to our observation occurred approximately 3 hours before the expected time based on the Hébrard et al. (2016) ephemeris. This is substantially larger than their reported uncertainty in T_{conj} , but is well within the uncertainty resulting from propagating the orbital period uncertainty to the observed epoch. This suggests that uncertainty in the orbital period of HD 143105 b is the primary contributor to the observed change in the conjunction time. A reduction of 0.1 minutes in the orbital period would entirely explain the change in conjunction time, and is compatible with the 0.4 minute period uncertainty reported in Hébrard et al. (2016). While our limited phase coverage prevents accurate revision of the orbital period, the revised conjunction time from the retrieval, $T_{\text{conj}} = 2456531.242^{+0.010}_{-0.012}$, will enable more precise timing of follow-up observations for the next several years. This demonstrates that high-resolution cross-correlation techniques do not necessarily require precise ephemeris knowledge, as long as a sufficiently large velocity shift is observed for the planet signal to be clearly detected in the $K_p - \Delta T_{\text{conj}}$ space.

HD 143105 b is non-transiting, so the orbital inclination and true mass were not known *a priori*. As the measured value of K_p is the radial projection of the total orbital velocity, it can be used to calculate the inclination as follows:

$$K_p = K_{p,max} \sin i = \frac{2\pi a}{T} \times \sin i \quad (2)$$

The semi-major axis a is not directly observable, but can be replaced using Kepler’s third law to give:

$$K_p = \sin i \times \left(\frac{2\pi GM_*}{T} \right)^{1/3} \quad (3)$$

Using the stellar mass and orbital period from Hébrard et al. (2016), we obtain $K_{p,max} = 187.9^{+4.4}_{-4.7}$ km s⁻¹, with the uncertainty dominated by the uncertainty in the stellar mass. We can then solve for the inclination:

$$\sin i = K_p / K_{p,max} = 0.98 \pm 0.07 \quad (4)$$

Which gives $i = 78^{+12}_{-12}$, restricting to $\sin i < 1$. While $\sin i$ is strictly < 1 , we have neglected the degeneracy between K_p and $K_{p,max}$ when propagating uncertainties, so $\sin i > 1$ appears to be compatible with the uncertainties despite being non-physical. Larger stellar masses increase $K_{p,max}$, permitting higher values of K_p , and inclusion of $\sin i > 1$ in the statistical error therefore suggests the stellar mass may be somewhat underestimated. A more informative upper bound can be obtained from the lack of a reported transit, which

requires $i < 80^\circ$ for the reported stellar parameters from Hébrard et al. (2016). We therefore adopt $i = 78^{+2}_{-12}$ as the inclination of the system. We can then determine the true planet mass by dividing the minimum mass obtained from radial velocity measurements by $\sin i$, yielding $M_{\text{true}} = 1.23 \pm 0.10 M_J$, including the $M \sin i$ uncertainty from Hébrard et al. (2016).

This result makes HD 143105 b one of a handful of non-transiting planets with a known true mass determined via high-resolution cross-correlation techniques (Brogi et al. 2012, 2014; Birkby et al. 2017; Guilluy et al. 2019). This is currently the only technique which can retrieve atmospheric properties for close-in, non-transiting planets.

4.2. Thermal structure

The retrieved posterior for the γ parameter, which determines whether the $P - T$ profile has a thermal inversion, strongly prefers a non-inverted structure, with a weak tail permitting inversions. This is potentially consistent with a weak, localized thermal inversion close to the substellar point marginally contributing to the observed flux. The apparently low C/O ratio of HD 143105 b significantly complicates efforts to confirm any inversion. `easyCHEM` chemical equilibrium models predict H₂O should rapidly dissociate in the thermal inversion, leaving CO as the only species with significant K -band opacity in the inverted region of the atmosphere. If the CO abundance is very low, as the retrieval analysis prefers, this may lead to a featureless K -band spectrum from any inverted region, preventing detection of that region with HRCCS.

The relatively edge-on retrieved inclination of HD 143105 b suggests the lack of an inversion is not simply an issue of viewing geometry. For a low-inclination (e.g. $i < 60^\circ$), our post-conjunction observations would be much more sensitive to morning longitudes and high latitudes compared with evening/equatorial regions. This could significantly decrease the visibility of a localized inversion, which models predict would occur near equatorial latitudes and substellar or afternoon longitudes (Roth et al. 2024). However, our analysis prefers $i \sim 78^\circ$ for HD 143105 b, and should therefore still be sensitive to equatorial latitudes, making it difficult to miss a thermal inversion of significant extent as a result of viewing geometry alone.

Observationally, thermal inversions are routinely seen in planets with equilibrium temperatures > 2200 K (e.g. Finnerty et al. 2023; Ramkumar et al. 2023, Finnerty et al., *subm.*), but not seen for temperatures < 1800 K (e.g. Line et al. 2021; Pelletier et al. 2021; Finnerty et al. 2024). Beyond these observations of HD 143105 b,

relatively few objects have been characterized in the 1800 – 2200 K range where this transition occurs. This makes HD 143105 b a potentially important object for understanding when and how thermal inversions form in exoplanet atmospheres.

For equilibrium temperatures > 2500 K, circulation models predict the presence of thermal inversion regardless of chemical composition (Lothringer et al. 2018). At lower temperatures, inversions are strongly associated with the presence of metal oxide species, particularly TiO and VO (e.g. Fortney et al. 2008). The abundances of these species can be significantly impacted by cold trapping (Hubeny et al. 2003), which may lead to localized inversions existing only where these species are in the gas phase. Nightside cold trapping of Ti has been reported in the UHJ WASP-76 b ($T_{\text{eq}} = 2200$ K Pelletier et al. 2023), but the details of this process are difficult to model, and the temperature at which thermal inversions form in typical hot Jupiters is unclear. Modeling by Roth et al. (2024) using 3D GCMs suggests the transition temperature to thermally-inverted $P - T$ profiles is ~ 1800 K in the presence of TiO/VO, while previous 1D modeling by Baxter et al. (2020) preferred an onset around 1700 K, but models omitting TiO/VO do not show inversions until substantially higher temperatures. These models predict that HD 143105 b, with an equilibrium temperature of ~ 1900 K, should have a dayside inversion only if significant quantities of TiO/VO are present.

Given the low retrieved metallicity of HD 143105 b, there may simply be insufficient TiO/VO in the atmosphere to produce a thermal inversion, especially if Ti is being cold-trapped on the nightside. TiO has substantially greater opacity in the H and J bands compared with K , which should allow the upcoming Keck/HISPEC instrument (Mawet et al. 2019) to either detect TiO or place a meaningful upper limit on its abundance. The revised ephemeris from this work will make it easier to obtain broad phase coverage in followup observations for phase-resolved retrievals. Such analysis will allow the partial inversion scenario to be definitively ruled out and will offer greater clarity into potential cold trapping impacting the TiO abundance.

4.3. C/O and metallicity

Derived posteriors for C/O, [C/H], [O/H], and [(C+O)/H] are shown in Figure 6. The oxygen abundance is sub-solar by ~ 1.3 dex at just over 1σ significance. The retrieval provides only an upper limit on the atmospheric mass fraction for CO, $\log CO < -3.7$ at 95% confidence. There is a weak, kinematically offset mode with very high CO and low H₂O abundance,

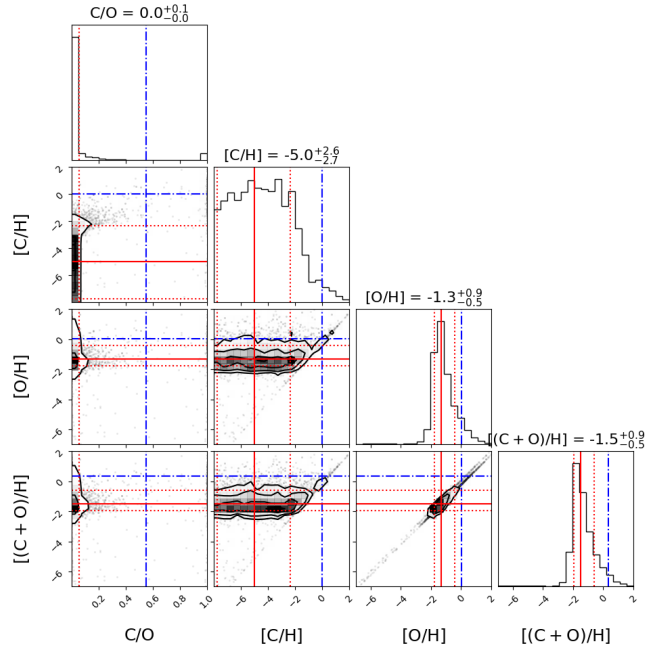


Figure 6. Corner plot showing the retrieved C/O, [C/H], [O/H], and [(C+O)/H] posteriors, computed from the retrieved abundances for H₂O and CO. Stellar values are indicated in dash-dot blue, while the retrieved median and $\pm 34\%$ confidence intervals are indicated in solid and dotted red, respectively. While the oxygen abundance is sub-solar/stellar at $\sim 1\sigma$, the carbon abundance is only an upper limit, leading to an upper limit on the C/O ratio. These results are consistent with a metal- and carbon-poor atmosphere for HD 143105 b.

which can be seen at the extreme right of the C/O posterior in Figure 6. As this mode is offset in both K_p and T_{conj} , we omit these points when estimating the upper limit on the C/O ratio. This leads to an upper limit on the C/O ratio, $C/O < 0.2$ at 95% confidence, while the maximum-likelihood value is $C/O = 0.1$ and the retrieved median is consistent with a nearly carbon-free atmosphere. The Bayes factor comparing the maximum-likelihood model with the same model omitting CO is only 2.9, consistent with a marginal preference for CO. This suggests the atmospheric CO abundance may be slightly below our detection threshold. Future observations with Keck/HISPEC (Mawet et al. 2019) will offer significant improvements in both instrument throughput and spectral resolution, which may enable precise constraints on the CO abundance and C/O ratio even in low-metallicity atmospheres. The continuous wavelength coverage of HISPEC may be particularly valuable in this case, as HISPEC observations will capture the full R and P branches associated with the $2.3\mu\text{m}$ CO bandhead, greatly increasing the number of observed CO lines compared with KPIC.

The low-C/O ratio, low-metallicity atmospheric composition our retrievals prefer for HD 143105 b has not previously been observed in an exoplanet atmosphere, and contradicts model predictions that these parameters should be inversely correlated (Espinoza et al. 2017; Cridland et al. 2019; Khorshid et al. 2022). In these models, oxygen enrichment usually arises from late planetesimal accretion, which should also increase the atmospheric metallicity. Low metallicity and low C/O ratio would require the accretion of significant quantities of oxygen-rich gas, but protoplanetary disk gas is generally carbon-rich as a result of condensation (Öberg et al. 2011). Chachan et al. (2023) finds that the region just beyond the H₂O snow line has substantially enriched H₂O ice relative to the rest of the disk, which could lead to an oxygen-rich atmosphere, although we would still expect a stellar or super-stellar metallicity in this scenario.

HRCCS observations have difficulty measuring absolute abundances due to the loss of continuum information during the data processing. As a result, we cannot conclusively rule out a stellar abundance of oxygen, and the C/H posterior similarly has a tail that extends to values compatible with the solar carbon abundance (see Figure 6). This alone could resolve the anomalous apparent composition of HD 143105 b. Furthermore, our estimate of the atmospheric metallicity is based only on abundances of volatile species. Inferring bulk metallicity from these species alone can be misleading due to either atmospheric effects, including oxygen bonding to refractory species (Lodders 2003), and cold trapping in the planetary atmosphere (Spiegel et al. 2009; Pelletier et al. 2023), or due to formation effects, including pebble drift and volatile trapping, which can alter the intrinsic refractory/volatile ratio (Booth et al. 2017; Ligtnerink et al. 2024; Lothringer et al. 2021; Chachan et al. 2023). Obtaining refractory species abundances can potentially resolve several of these scenarios by constraining the solid accretion history of a planet (Lothringer et al. 2021; Chachan et al. 2023), but will require additional observations in the case of HD 143105 b.

This unusual composition for HD 143105 b is consistent with the emerging picture of significant chemical diversity in the hot Jupiter population (Kempton & Knutson 2024; Wisner et al. 2024). Reported metallicities for various exoplanets range from very high (e.g. Bean et al. 2023) to moderately super-solar (e.g. Finnerty et al. 2024; Fu et al. 2024) to sub-solar (e.g. Line et al. 2021; August et al. 2023; Weiner Mansfield et al. 2024). Similarly, reported C/O ratios range from substantially sub-stellar (e.g. Finnerty et al. 2024; Fu et al. 2024) to significantly carbon-enriched (Finnerty et al. submitted),

although in the case of ultra-hot Jupiters constraining the C/O ratio is complicated by the impact of molecular dissociation (Brogi et al. 2023; Ramkumar et al. 2023; Gandhi et al. 2024). This diversity suggests a variety of formation and evolutionary processes shape the hot Jupiter population, motivating further observations and improvements in retrieval techniques to incorporate a broader range of data, such as joint optical/infrared and high/low resolution retrievals.

5. SUMMARY AND CONCLUSIONS

We detected atmospheric H₂O absorption from the non-transiting hot Jupiter HD 143105 b. Cross-correlation analysis indicates the conjunction time is 2.5 hours earlier than the published ephemeris, likely due to the accumulation of uncertainty in the orbital period over nearly a decade. The planet radial velocity semi-amplitude is $K_p = 185_{-13}^{+11} \text{ km s}^{-1}$, giving an orbital inclination of 78_{-12}^{+2} and a true planet mass of $1.23 \pm 0.10 M_J$, with an upper inclination limit imposed by the absence of a transit detection. This is the first non-transiting hot Jupiter detected with KPIC and the first atmospheric detection of HD 143105 b.

While the equilibrium temperature of HD 143105 b is in the transition regime between non-inverted and inverted atmospheres, our analysis strongly prefers a non-inverted $P - T$ profile. This is unlikely to be solely the result of viewing geometry given the high inclination of HD 143105 b, suggesting that the lack of an inversion may be a result of low bulk metallicity leading to low abundances of inversion-causing species such as TiO and VO. Additional observations with broader wavelength coverage would greatly improve sensitivity to these species and directly test this explanation. HD 143105 b is potentially a key benchmark object for understanding the transition between inverted and non-inverted exoplanet atmospheres.

Retrieval analysis provides a bounded constraint on the H₂O mass-mixing ratio $\log \text{H}_2\text{O} = -3.9_{-0.5}^{+0.8}$ and a 95% upper limit on the CO mass-mixing ratio $\log \text{CO} < -3.7$. This places an upper limit on the C/O ratio $\text{C/O} < 0.2$ at 95% confidence, and suggests a sub-solar atmospheric metallicity. This combination of low metallicity and low C/O ratio is unusual in exoplanet atmospheres and has not been seen previously in high-resolution retrievals, but is consistent with other findings suggesting a chemically diverse hot Jupiter population. Future observations with Keck/HISPEC will have wider wavelength coverage and improved spectral resolution, which may be sufficient to detect CO in HD 143105 band establish a bounded constraint on the C/O ratio. Such observations may also provide con-

straints on refractory species such as iron or magnesium, which may clarify the formation history of HD 143105 b through constraining the refractory-to-volatile ratio.

Finally, observations with higher spectral resolution and/or wider phase coverage may enable detection of phase-dependent velocity shifts relative to a Keplerian orbit. Such shifts would offer insight into atmospheric circulation patterns, which are particularly interesting for non-transiting planets such as HD 143105 b, as the observed emission probes higher latitudes compared with transiting planets. In the future, high-resolution spectroscopy of non-transiting planets may be a unique tool for probing atmospheric circulation patterns in polar regions of hot giant planets.

We thank the anonymous referee whose thoughtful comments improved the quality of this paper. L. F. is a member of UAW local 4811. L.F. acknowledges the support of the W.M. Keck Foundation, which also supports development of the KPIC facility data reduction pipeline. The contributed Hoffman2 computing node used for this work was supported by the Heising-Simons Foundation grant #2020-1821. Funding for KPIC has been provided by the California Institute of Technology, the Jet Propulsion Laboratory, the Heising-Simons Foundation (grants #2015-129, #2017-318, #2019-1312, #2023-4597, #2023-4598), the Simons Foundation (through the Caltech Center for Comparative Planetary Evolution), and the NSF under grant AST-1611623. D.E. acknowledges support from the NASA Future Investigators in NASA Earth and Space Science and Technology (FINESST) fellowship under award #80NSSC19K1423, as well as support from the Keck Visiting Scholars Program (KVSP) to install the Phase II upgrades for KPIC. J.X. acknowledges support from the NASA Future Investigators in NASA Earth and Space Science and Technology (FINESST) award #80NSSC23K1434.

This work used computational and storage services associated with the Hoffman2 Shared Cluster provided by UCLA Institute for Digital Research and Education's Research Technology Group. L.F. thanks Briley Lewis for her helpful guide to using Hoffman2, and Paul Mollière for his assistance in adding additional opacities to petitRADTRANS.

The data presented herein were obtained at the W. M. Keck Observatory, which is operated as a scientific partnership among the California Institute of Technology, the University of California and the National Aeronautics and Space Administration. The Observatory was made possible by the generous financial support of the W. M. Keck Foundation. W. M. Keck Observatory access was supported by Northwestern University and the Center for Interdisciplinary Exploration and Research in Astrophysics (CIERA). The authors wish to recognize and acknowledge the very significant cultural role and reverence that the summit of Mauna Kea has always had within the indigenous Hawaiian community. We are most fortunate to have the opportunity to conduct observations from this mountain.

This research has made use of the NASA Exoplanet Archive, which is operated by the California Institute of Technology, under contract with the National Aeronautics and Space Administration under the Exoplanet Exploration Program. The research shown here acknowledges use of the Hypatia Catalog Database, an online compilation of stellar abundance data as described in Hinkel et al. (2014, *AJ*, 148, 54), which was supported by NASA's Nexus for Exoplanet System Science (NExSS) research coordination network and the Vanderbilt Initiative in Data-Intensive Astrophysics (VIDA).

Facilities: Keck:II(NIRSPEC/KPIC)

Software: `astropy` (Astropy Collaboration et al. 2013, 2018), `dynesty` (Speagle 2020), `corner` (Foreman-Mackey 2016), `petitRADTRANS` (Mollière et al. 2019, 2020)

APPENDIX

A. CORNER PLOTS

Figure 7 presents the full corner plot from the retrieval.

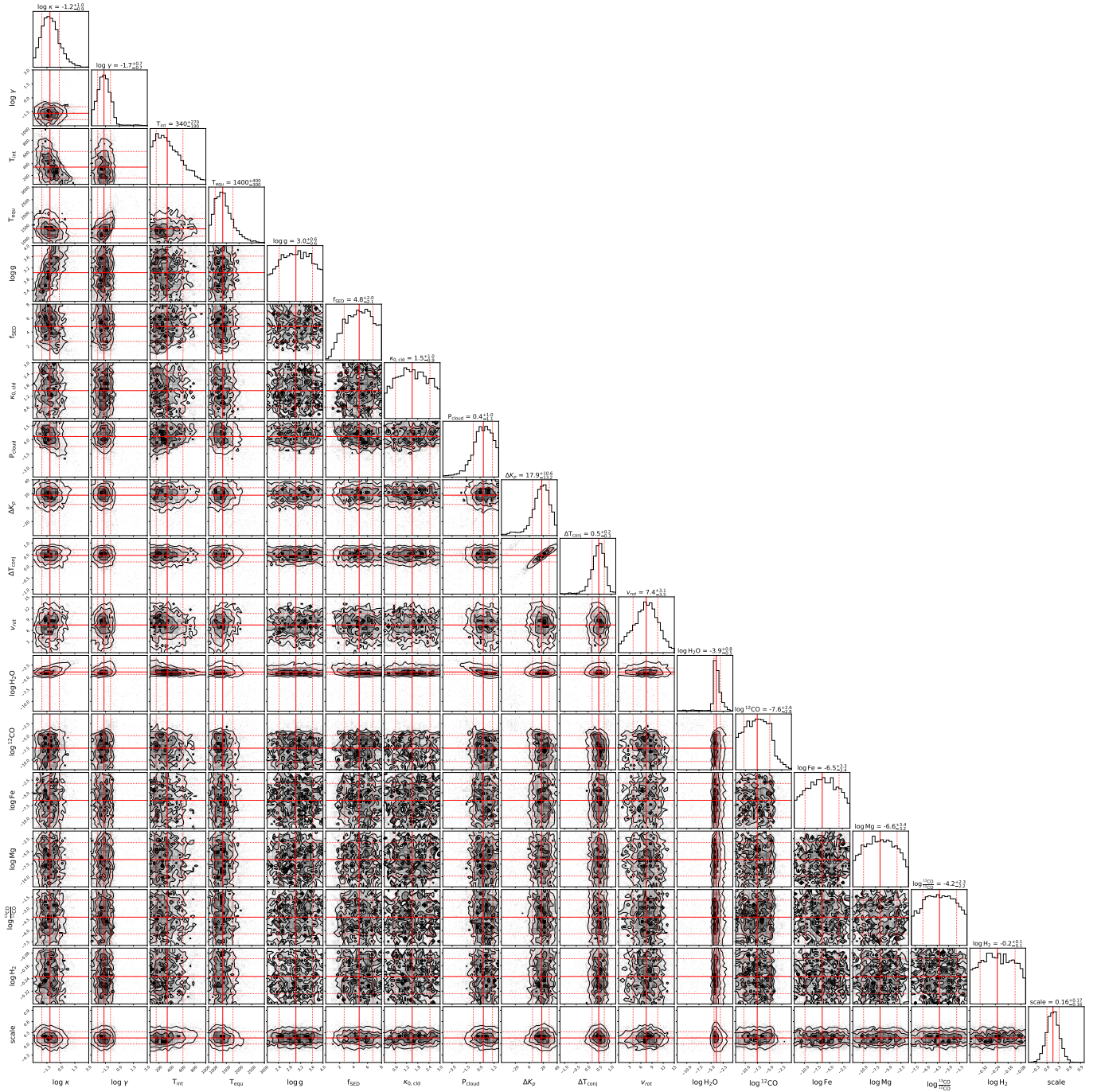


Figure 7. Full corner plot for the 6-component retrieval.

REFERENCES

- Astropy Collaboration, Robitaille, T. P., Tollerud, E. J., et al. 2013, *A&A*, 558, A33, doi: [10.1051/0004-6361/201322068](https://doi.org/10.1051/0004-6361/201322068)
- Astropy Collaboration, Price-Whelan, A. M., Sipőcz, B. M., et al. 2018, *AJ*, 156, 123, doi: [10.3847/1538-3881/aabc4f](https://doi.org/10.3847/1538-3881/aabc4f)
- August, P. C., Bean, J. L., Zhang, M., et al. 2023, *ApJL*, 953, L24, doi: [10.3847/2041-8213/ace828](https://doi.org/10.3847/2041-8213/ace828)
- Baxter, C., Désert, J.-M., Parmentier, V., et al. 2020, *A&A*, 639, A36, doi: [10.1051/0004-6361/201937394](https://doi.org/10.1051/0004-6361/201937394)
- Bean, J. L., Xue, Q., August, P. C., et al. 2023, *Nature*, 618, 43, doi: [10.1038/s41586-023-05984-y](https://doi.org/10.1038/s41586-023-05984-y)
- Birkby, J. L., de Kok, R. J., Brogi, M., Schwarz, H., & Snellen, I. A. G. 2017, *AJ*, 153, 138, doi: [10.3847/1538-3881/aa5c87](https://doi.org/10.3847/1538-3881/aa5c87)
- Booth, R. A., Clarke, C. J., Madhusudhan, N., & Ilee, J. D. 2017, *MNRAS*, 469, 3994, doi: [10.1093/mnras/stx1103](https://doi.org/10.1093/mnras/stx1103)
- Brogi, M., de Kok, R. J., Birkby, J. L., Schwarz, H., & Snellen, I. A. G. 2014, *A&A*, 565, A124, doi: [10.1051/0004-6361/201423537](https://doi.org/10.1051/0004-6361/201423537)
- Brogi, M., & Line, M. R. 2019, *AJ*, 157, 114, doi: [10.3847/1538-3881/aaffd3](https://doi.org/10.3847/1538-3881/aaffd3)
- Brogi, M., Snellen, I. A. G., de Kok, R. J., et al. 2012, *Nature*, 486, 502, doi: [10.1038/nature11161](https://doi.org/10.1038/nature11161)
- Brogi, M., Snellen, I. A. G., de Kok, R. J., et al. 2013, *ApJ*, 767, 27, doi: [10.1088/0004-637X/767/1/27](https://doi.org/10.1088/0004-637X/767/1/27)
- Brogi, M., Emeka-Okafor, V., Line, M. R., et al. 2023, *AJ*, 165, 91, doi: [10.3847/1538-3881/acaf5c](https://doi.org/10.3847/1538-3881/acaf5c)
- Buchner, J., Georgakakis, A., Nandra, K., et al. 2014, *A&A*, 564, A125, doi: [10.1051/0004-6361/201322971](https://doi.org/10.1051/0004-6361/201322971)
- Buzard, C., Finnerty, L., Piskorz, D., et al. 2020, *AJ*, 160, 1, doi: [10.3847/1538-3881/ab8f9c](https://doi.org/10.3847/1538-3881/ab8f9c)
- Chachan, Y., Knutson, H. A., Lothringer, J., & Blake, G. A. 2023, *ApJ*, 943, 112, doi: [10.3847/1538-4357/aca614](https://doi.org/10.3847/1538-4357/aca614)
- Cridland, A. J., van Dishoeck, E. F., Alessi, M., & Pudritz, R. E. 2019, *A&A*, 632, A63, doi: [10.1051/0004-6361/201936105](https://doi.org/10.1051/0004-6361/201936105)
- Cutri, R. M., Skrutskie, M. F., van Dyk, S., et al. 2003, *VizieR Online Data Catalog*, II/246
- Delorme, J.-R., Jovanovic, N., Echeverri, D., et al. 2021, *Journal of Astronomical Telescopes, Instruments, and Systems*, 7, 035006, doi: [10.1117/1.JATIS.7.3.035006](https://doi.org/10.1117/1.JATIS.7.3.035006)
- Echeverri, D., Jovanovic, N., Delorme, J.-R., et al. 2022, in *Ground-based and Airborne Instrumentation for Astronomy IX*, ed. C. J. Evans, J. J. Bryant, & K. Motohara, Vol. 12184, International Society for Optics and Photonics (SPIE), 121841W, doi: [10.1117/12.2630518](https://doi.org/10.1117/12.2630518)
- Espinoza, N., Fortney, J. J., Miguel, Y., Thorngren, D., & Murray-Clay, R. 2017, *ApJL*, 838, L9, doi: [10.3847/2041-8213/aa65ca](https://doi.org/10.3847/2041-8213/aa65ca)
- ExoFOP. 2019, Exoplanet Follow-up Observing Program - TESS, IPAC, doi: [10.26134/EXOFOP3](https://doi.org/10.26134/EXOFOP3)
- Feroz, F., & Hobson, M. P. 2008, *MNRAS*, 384, 449, doi: [10.1111/j.1365-2966.2007.12353.x](https://doi.org/10.1111/j.1365-2966.2007.12353.x)
- Feroz, F., Hobson, M. P., & Bridges, M. 2009, *MNRAS*, 398, 1601, doi: [10.1111/j.1365-2966.2009.14548.x](https://doi.org/10.1111/j.1365-2966.2009.14548.x)
- Feroz, F., Hobson, M. P., Cameron, E., & Pettitt, A. N. 2019, *The Open Journal of Astrophysics*, 2, 10, doi: [10.21105/astro.1306.2144](https://doi.org/10.21105/astro.1306.2144)
- Finnerty, L., Schofield, T., Delorme, J.-R., et al. 2022, in *Ground-based and Airborne Instrumentation for Astronomy IX*, ed. C. J. Evans, J. J. Bryant, & K. Motohara, Vol. 12184, International Society for Optics and Photonics (SPIE), 121844Y, doi: [10.1117/12.2630276](https://doi.org/10.1117/12.2630276)
- Finnerty, L., Schofield, T., Sappey, B., et al. 2023, *AJ*, 166, 31, doi: [10.3847/1538-3881/acda91](https://doi.org/10.3847/1538-3881/acda91)
- Finnerty, L., Xuan, J. W., Xin, Y., et al. 2024, *AJ*, 167, 43, doi: [10.3847/1538-3881/ad1180](https://doi.org/10.3847/1538-3881/ad1180)
- Foreman-Mackey, D. 2016, *The Journal of Open Source Software*, 1, 24, doi: [10.21105/joss.00024](https://doi.org/10.21105/joss.00024)
- Fortney, J. J., Lodders, K., Marley, M. S., & Freedman, R. S. 2008, *ApJ*, 678, 1419, doi: [10.1086/528370](https://doi.org/10.1086/528370)
- Fu, G., Welbanks, L., Deming, D., et al. 2024, *arXiv e-prints*, arXiv:2407.06163, doi: [10.48550/arXiv.2407.06163](https://doi.org/10.48550/arXiv.2407.06163)
- Gaia Collaboration. 2020, *VizieR Online Data Catalog*, I/350
- Gandhi, S., Landman, R., Snellen, I., et al. 2024, *MNRAS*, 530, 2885, doi: [10.1093/mnras/stae1048](https://doi.org/10.1093/mnras/stae1048)
- Gandhi, S., Kesseli, A., Zhang, Y., et al. 2023, *AJ*, 165, 242, doi: [10.3847/1538-3881/accd65](https://doi.org/10.3847/1538-3881/accd65)
- Gordon, I. E., Rothman, L. S., Hargreaves, R. J., et al. 2022, *JQSRT*, 277, 107949, doi: [10.1016/j.jqsrt.2021.107949](https://doi.org/10.1016/j.jqsrt.2021.107949)
- Guillot, T. 2010, *A&A*, 520, A27, doi: [10.1051/0004-6361/200913396](https://doi.org/10.1051/0004-6361/200913396)
- Guilluy, G., Sozzetti, A., Brogi, M., et al. 2019, *A&A*, 625, A107, doi: [10.1051/0004-6361/201834615](https://doi.org/10.1051/0004-6361/201834615)
- Hébrard, G., Arnold, L., Forveille, T., et al. 2016, *A&A*, 588, A145, doi: [10.1051/0004-6361/201527585](https://doi.org/10.1051/0004-6361/201527585)
- Hinkel, N. R., Timmes, F. X., Young, P. A., Pagano, M. D., & Turnbull, M. C. 2014, *AJ*, 148, 54, doi: [10.1088/0004-6256/148/3/54](https://doi.org/10.1088/0004-6256/148/3/54)
- Hubeny, I., Burrows, A., & Sudarsky, D. 2003, *ApJ*, 594, 1011, doi: [10.1086/377080](https://doi.org/10.1086/377080)
- Kempton, E. M. R., & Knutson, H. A. 2024, *Reviews in Mineralogy and Geochemistry*, 90, 411, doi: [10.2138/rmg.2024.90.12](https://doi.org/10.2138/rmg.2024.90.12)

- Khorshid, N., Min, M., Désert, J. M., Woitke, P., & Dominik, C. 2022, *A&A*, 667, A147, doi: [10.1051/0004-6361/202141455](https://doi.org/10.1051/0004-6361/202141455)
- Lei, E., & Mollière, P. 2024, arXiv e-prints, arXiv:2410.21364, doi: [10.48550/arXiv.2410.21364](https://doi.org/10.48550/arXiv.2410.21364)
- Li, G., Gordon, I. E., Rothman, L. S., et al. 2015, *ApJS*, 216, 15, doi: [10.1088/0067-0049/216/1/15](https://doi.org/10.1088/0067-0049/216/1/15)
- Ligterink, N. F. W., Kipfer, K. A., & Gavino, S. 2024, *A&A*, 687, A224, doi: [10.1051/0004-6361/202450405](https://doi.org/10.1051/0004-6361/202450405)
- Line, M. R., Brogi, M., Bean, J. L., et al. 2021, *Nature*, 598, 580, doi: [10.1038/s41586-021-03912-6](https://doi.org/10.1038/s41586-021-03912-6)
- Lodders, K. 2003, *ApJ*, 591, 1220, doi: [10.1086/375492](https://doi.org/10.1086/375492)
- López, R. A., Hoffman, E. B., Doppmann, G., et al. 2020, in *Society of Photo-Optical Instrumentation Engineers (SPIE) Conference Series*, Vol. 11447, Society of Photo-Optical Instrumentation Engineers (SPIE) Conference Series, 114476B, doi: [10.1117/12.2563075](https://doi.org/10.1117/12.2563075)
- Lothringer, J. D., Barman, T., & Koskinen, T. 2018, *ApJ*, 866, 27, doi: [10.3847/1538-4357/aadd9e](https://doi.org/10.3847/1538-4357/aadd9e)
- Lothringer, J. D., Rustamkulov, Z., Sing, D. K., et al. 2021, *ApJ*, 914, 12, doi: [10.3847/1538-4357/abf8a9](https://doi.org/10.3847/1538-4357/abf8a9)
- Malsky, I., Rauscher, E., Kempton, E. M. R., et al. 2021, *ApJ*, 923, 62, doi: [10.3847/1538-4357/ac2a2a](https://doi.org/10.3847/1538-4357/ac2a2a)
- Martin, E. C., Fitzgerald, M. P., McLean, I. S., et al. 2018, in *Society of Photo-Optical Instrumentation Engineers (SPIE) Conference Series*, Vol. 10702, Ground-based and Airborne Instrumentation for Astronomy VII, ed. C. J. Evans, L. Simard, & H. Takami, 107020A, doi: [10.1117/12.2312266](https://doi.org/10.1117/12.2312266)
- Mawet, D., Fitzgerald, M., Konopacky, Q., et al. 2019, arXiv e-prints, doi: [10.48550/ARXIV.1908.03623](https://doi.org/10.48550/ARXIV.1908.03623)
- McLean, I. S., Becklin, E. E., Bendiksen, O., et al. 1998, in *Society of Photo-Optical Instrumentation Engineers (SPIE) Conference Series*, Vol. 3354, Infrared Astronomical Instrumentation, ed. A. M. Fowler, 566–578, doi: [10.1117/12.317283](https://doi.org/10.1117/12.317283)
- Mollière, P., van Boekel, R., Bouwman, J., et al. 2017, *A&A*, 600, A10, doi: [10.1051/0004-6361/201629800](https://doi.org/10.1051/0004-6361/201629800)
- Mollière, P., Wardenier, J. P., van Boekel, R., et al. 2019, *A&A*, 627, A67, doi: [10.1051/0004-6361/201935470](https://doi.org/10.1051/0004-6361/201935470)
- Mollière, P., Stolker, T., Lacour, S., et al. 2020, *A&A*, 640, A131, doi: [10.1051/0004-6361/202038325](https://doi.org/10.1051/0004-6361/202038325)
- Nasedkin, E., Mollière, P., & Blain, D. 2024, *Journal of Open Source Software*, 9, 5875, doi: [10.21105/joss.05875](https://doi.org/10.21105/joss.05875)
- Öberg, K. I., Murray-Clay, R., & Bergin, E. A. 2011, *ApJL*, 743, L16, doi: [10.1088/2041-8205/743/1/L16](https://doi.org/10.1088/2041-8205/743/1/L16)
- Pai Asnodkar, A., Wang, J., Eastman, J. D., et al. 2022, *AJ*, 163, 155, doi: [10.3847/1538-3881/ac51d2](https://doi.org/10.3847/1538-3881/ac51d2)
- Pelletier, S., Benneke, B., Darveau-Bernier, A., et al. 2021, *AJ*, 162, 73, doi: [10.3847/1538-3881/ac0428](https://doi.org/10.3847/1538-3881/ac0428)
- Pelletier, S., Benneke, B., Ali-Dib, M., et al. 2023, *Nature*, 619, 491, doi: [10.1038/s41586-023-06134-0](https://doi.org/10.1038/s41586-023-06134-0)
- Polyansky, O. L., Kyuberis, A. A., Zobov, N. F., et al. 2018, *MNRAS*, 480, 2597, doi: [10.1093/mnras/sty1877](https://doi.org/10.1093/mnras/sty1877)
- Ramkumar, S., Gibson, N. P., Nugroho, S. K., Maguire, C., & Fortune, M. 2023, *MNRAS*, 525, 2985, doi: [10.1093/mnras/stad2476](https://doi.org/10.1093/mnras/stad2476)
- Rodler, F., Lopez-Morales, M., & Ribas, I. 2012, *ApJL*, 753, L25, doi: [10.1088/2041-8205/753/1/L25](https://doi.org/10.1088/2041-8205/753/1/L25)
- Roth, A., Parmentier, V., & Hammond, M. 2024, *MNRAS*, 531, 1056, doi: [10.1093/mnras/stae984](https://doi.org/10.1093/mnras/stae984)
- Rothman, L. S., Gordon, I. E., Barber, R. J., et al. 2010, *JQSRT*, 111, 2139, doi: [10.1016/j.jqsrt.2010.05.001](https://doi.org/10.1016/j.jqsrt.2010.05.001)
- Speagle, J. S. 2020, *MNRAS*, 493, 3132, doi: [10.1093/mnras/staa278](https://doi.org/10.1093/mnras/staa278)
- Spiegel, D. S., Silverio, K., & Burrows, A. 2009, *ApJ*, 699, 1487, doi: [10.1088/0004-637X/699/2/1487](https://doi.org/10.1088/0004-637X/699/2/1487)
- Webb, R. K., Brogi, M., Gandhi, S., et al. 2020, *MNRAS*, 494, 108, doi: [10.1093/mnras/staa715](https://doi.org/10.1093/mnras/staa715)
- Weiner Mansfield, M., Line, M. R., Wardenier, J. P., et al. 2024, *AJ*, 168, 14, doi: [10.3847/1538-3881/ad4a5f](https://doi.org/10.3847/1538-3881/ad4a5f)
- Wiser, L. S., Line, M. R., Welbanks, L., et al. 2024, *ApJ*, 971, 33, doi: [10.3847/1538-4357/ad5097](https://doi.org/10.3847/1538-4357/ad5097)